Energy & Environmental Science

Tailoring the Structural Durability and Proton Conduction of Electrolytes for Highly Fuel-flexible and Reversible Ceramic Cells

Journal:	*Energy & Environmental Science*
Manuscript ID	EE-ART-03-2025-001318.R1
Article Type:	Paper
Date Submitted by the Author:	07-May-2025
Complete List of Authors:	He, Fan; South China University of Technology School of Environment and Energy Huang, Yixuan; South China University of Technology Xu, Kang; South China University of Technology Xu, Yangsen; South China University of Technology Zhu, Feng; South China University of Technology, School of Environment and Energy Guo, Shihang; Soochow University Han, Donglin; Soochow University, College of Energy Tao, Haoliang; Ningbo Institute of Materials Technology and Engineering Chinese Academy of Sciences Zhu, Liangzhu; Ningbo Institute of Materials Technology and Engineering Chinese Academy of Sciences, New Energy Technology Sasaki, Kotaro; Brookhaven National Laboratory, Chemistry Choi, YongMan; National Yang Ming Chiao Tung University Shao, Zongping; Curtin University Chen, Yu; South China University of Technology

Broader context

Protonic ceramic cells (PCCs) can be efficiently operated in dual modes of fuel cell and electrolysis cell, with high fuel flexibility and operational reversibility. The development of electrolyte materials with high ionic conductivity and good durability is extremely important for low-temperature operation, efficiency, electrolysis/fuel cell cycling, and multi-fuel power generation. Here, we report a new electrolyte material $BaZr_{0.06}Ce_{0.7}Y_{0.06}Yb_{0.06}Hf_{0.06}Gd_{0.06}O_{3-\delta}$ (BZCYYbHG) with high conductivity and stability for PCCs. The activity and robustness of cells under operation conditions are demonstrated using the BZCYYbHG electrolyte and Ni-BZCYYbHG fuel electrode in fuel-cell mode fueled by H_2, NH_3, and CH_4, and electrolysis mode exposed to highly humid air and air containing CO_2. The developed electrolyte offers great potential for fabricating high-performance and durable PCC with high fuel flexibility and reversibility.

Tailoring the Structural Durability and Proton Conduction of Electrolytes for Highly Fuel-flexible and Reversible Ceramic Cells

Fan He[1], Yixuan Huang[1], Kang Xu[1], Yangsen Xu[1], Feng Zhu[1], Shihang Guo[2], Donglin Han[2], Haoliang Tao[3], Liangzhu Zhu[3], Kotaro Sasaki[4], YongMan Choi[5]*, Zongping Shao[6]*, and Yu Chen[1]*

[1]School of Environment and Energy, South China University of Technology, 382 East Road, Higher Education Mega Center, Guangzhou 510006, P. R. China.

[2]College of Energy, Soochow University, No 1 Shizi Street, Gusu District, Suzhou, 215006, China.

[3]Zhejiang Key Laboratory of Advanced Fuel Cells and Electrolyzers Technology, Ningbo Institute of Materials Technology and Engineering, Chinese Academy of Sciences, Ningbo, Zhejiang, 315200, PR China

[4]Chemistry Division, Brookhaven National Laboratory, Upton, NY 11973, USA

[5]College of Photonics, National Yang Ming Chiao Tung University, Tainan 71150, Taiwan

[6]WA School of Mines: Minerals, Energy and Chemical Engineering (WASM–MECE), Curtin University, Perth, WA 6102, Australia

*Corresponding authors. Email: YongMan Choi (ymchoi@nycu.edu.tw); Zongping Shao (zongping.shao@curtin.edu.au); Yu Chen (eschenyu@scut.edu.cn)

Abstract

A durable and high ionic conducting electrolyte is critical for achieving fuel-flexible and reversible protonic ceramic cells (PCCs) at reduced temperatures since the developed electrolyte materials are vulnerable to steam, CO_2, or coking deterioration. Here, we report a fast-conducting electrolyte material $BaZr_{0.06}Ce_{0.7}Y_{0.06}Yb_{0.06}Hf_{0.06}Gd_{0.06}O_{3-\delta}$ (BZCYYbHG), demonstrating excellent durability against CO_2 and H_2O under the realistic electrolysis operations, and a high conductivity of 0.017 S cm^{-1} at 550 °C for lowering the PCC operating temperature. Density functional theory calculations indicate that the higher configurational entropy of mixing at the B-site cations slightly reduces the hydrogen adsorption energy, suggesting a higher incorporation rate of protons or hydrogen atoms into the electrolyte bulk. Ultimately, single cells with BZCYYbHG electrolyte deliver peak power densities of 1.39, 1.12, and 0.7 W cm^{-2} in H_2, NH_3, and CH_4 at 550 °C with promising durability. In addition, the PCCs achieve a current density of -1.61 A cm^{-2} at 1.3 V and 550 °C with a high Faradaic efficiency of 91.3% at -0.5 A cm^{-2}, enabling stable operations in steam electrolysis mode under humid air (30% H_2O), wet air containing CO_2 (up to 10%), and reversible cycling.

Keywords: Protonic ceramic cells; Electrolyte; Fuel flexibility; Durability; Reversibility.

Main Text:

Unlike polymer electrolyte fuel cells, ceramic cells can operate in dual modes of fuel-cell (for energy conversion) and electrolyzer (for energy storage) on the same materials/catalysts with high fuel flexibility and operational reversibility.[1-5] Among the various components of ceramic cells, electrolyte materials for ionic conduction and fuel-oxidant separations are extremely important to cell operations. However, current ceramic electrolytes, including oxygen ion and proton conductors, face grand challenges like poor low-temperature conductivity and instability, especially in hydrocarbon fuels, high-concentration steam, and/or CO_2 poisoning under realistic

operation conditions.[6, 7] One key opportunity for achieving fuel flexibility and reversibility is to strengthen the stability of the electrolyte materials while maintaining high efficiency of ionic conduction at low operating temperatures to prolong the cell lifetime.

Over the last decades, tremendous progress has been made in advancing electrolytes for ceramic cells.[6, 8] The problems in safety and long-term stability caused by inevitable electron (e^-) conduction have been barriers for typical samarium/gadolinium doped cerium (SDC and GDC) electrolytes in large-scale commercialization.[9] The yttria-stabilized zirconia (YSZ) and $La_xSr_{1-x}Ga_yMg_{1-y}O_{3-\delta}$ electrolytes exhibit excellent structural stability and enough ionic conductivity (~0.01 S cm^{-1} at 700 °C). However, high-temperature operation (≥ 700 °C) becomes an insurmountable limit for their applications.[10, 11] The outstanding strides of low activation energy (~0.45 eV) and high ionic conductivity at low temperatures (≤ 600 °C) led to the fast development of proton-conducting electrolytes, which are now the dominant research focus.[12] The $BaZr_{0.1}Ce_{0.7}Y_{0.1}Yb_{0.1}O_{3-\delta}$ (BZCYYb) perovskite oxide has proven to be an excellent electrolyte in protonic ceramic cells (PCCs) with high ionic conductivity at low temperature (e.g., 0.01 S cm^{-2} at 500 °C).[10, 13-15] Nevertheless, the structural stability of BZCYYb electrolyte needs to be urgently improved when encountered in PCCs under harsh operating conditions of humid, CO_2, ammonia, and/or hydrocarbons.[16, 17] An interesting finding is that the structurally complete BZCYYb electrolyte via the special calcining technique could show enhanced conductivity and stability, implying that bulk element segregation is likely to be a key factor for the discrepancies in conductivity.[16, 17] Material designs of non-redox dopants (Zr, Nb, Ta, Hf, and W) have been proposed to improve the structural stability but at the sacrifice of ionic conductivity and sintering temperature.[18, 19] The presence of trivalent cations (e.g., Gd, Yb, Er, Y, Sm) in the perovskite electrolyte has shown the potential to create more oxygen vacancies, thereby promoting the formation of proton defects via the hydration reaction.[20-22] A trade-off should be possessed in tuning the stability and electrochemical performance of proton conductor electrolytes in PCCs.

While investigations have focused on tailoring the enthalpic interactions between non-redox cations and lanthanide species,[18, 23-25] the mixing entropy (ΔS_{mix}) as a design knob has significantly attracted less attention in developing PCC electrolytes. Increasing system entropy can decrease the free Gibbs energy of perovskite ceramics, which may enhance the structural stability.[26] Entropy engineering has been leveraged to modulate the performance and durability in many scientific fields of electrochemical catalysis, thermoelectricity, corrosion-resistant materials, energy utilization, and storage.[27-29] In an ABO_3-type perovskite system, the entropic driving force improves mechanical and functional properties by increasing cation diversity at the same site (A, B, and O sites).[27] Thus, unexpected electrochemical properties and stability of electrolytes can be attained by utilizing the entropy principle and tuning the properties of the components. Although experimental-related investigations are rare and the entropy-associated kinetics are complex, the properties of entropy electrolytes should be systematically studied, especially in realistic PCC operations.

Recently, Gd-doped proton-conducting electrolytes demonstrated promising conductivity and durability.[25] Although hafnium (Hf) has a relatively higher cost and similar ionic radius compared to zirconium (Zr), reactions with CO_2 and H_2O have been proven more difficult for Hf.[23, 30] Inspired by these, we design a perovskite electrolyte material with a formula of $BaZr_{0.06}Ce_{0.7}Y_{0.06}Yb_{0.06}Hf_{0.06}Gd_{0.06}O_{3-\delta}$ (BZCYYbHG) for fabricating high-performance and durable PCCs. We demonstrate the correlations between the mixing entropy (ΔS_{mix}) of electrolytes and ionic conductivity, proton diffusion mechanism, sinterability, bulk and grain boundary resistances, and chemical stability. When the BZCYYbHG is applied as electrolyte and anode ceramics with NiO for PCCs, the BZCYYbHG cells display a high peak power density of 1.39 W cm^{-2} at 550 °C and a current density of -1.61 A cm^{-2} at 1.3V and 550 °C. The BZCYYbHG cells also achieve excellent power output on NH_3 and wet CH_4. Furthermore, our PCCs show remarkable stabilities in fuel-cell mode at 550 °C fueled by H_2, NH_3, and wet CH_4, steam electrolysis mode at 600 °C, and reversible cycling at 550 °C.

Results and discussion

Evaluation of sintering performance and chemical stability

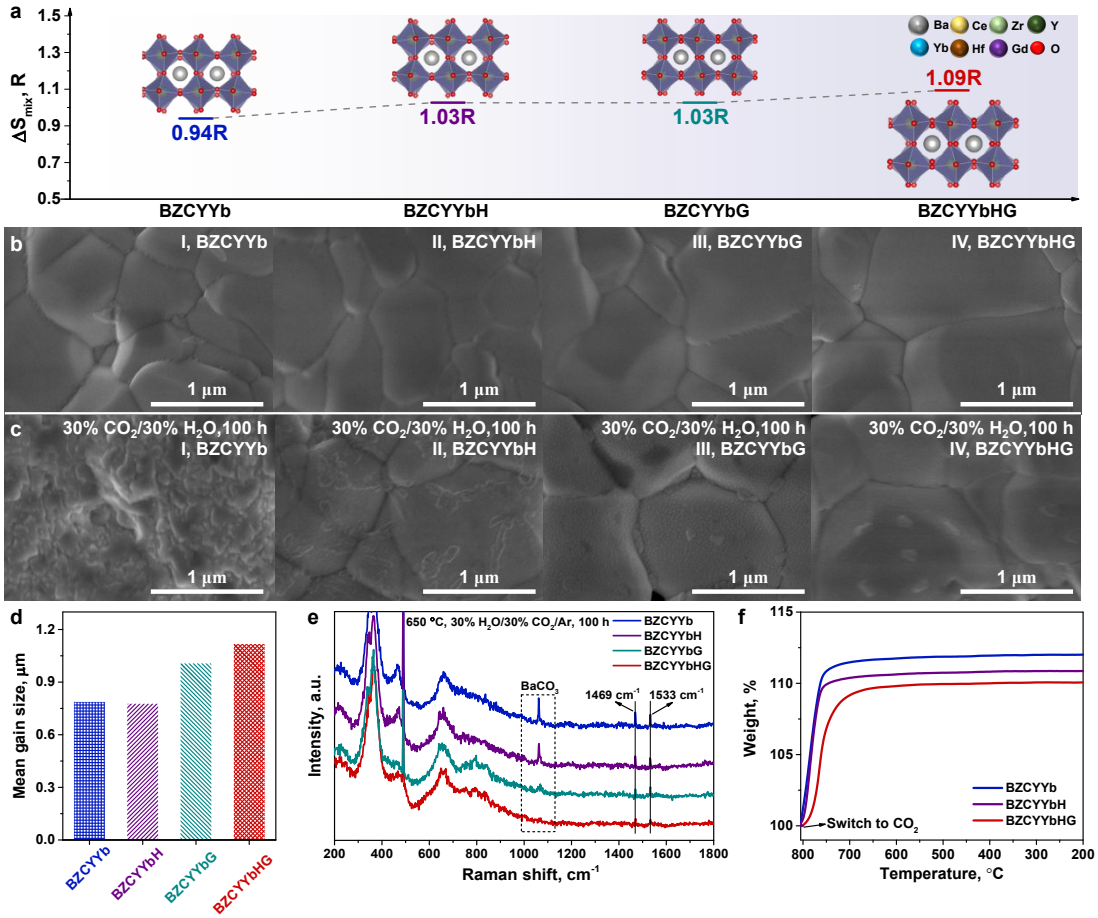

Figure 1. Sintering performance and chemical stability of electrolytes. (a) Entropy (ΔS_{mix}) and structural schematic of BZCYYb, BZCYYbH, BZCYYbG, and BZCYYbHG electrolytes; **(b)** Surface SEM images of the BZCYYb (I), BZCYYbH (II), BZCYYbG (III), and BZCYYbHG (IV) electrolytes before and **(c)** after interacted with the 30% CO_2 and 30% H_2O in Ar at 650 °C for 100 h; **(d)** The mean grain size of BZCYYb, BZCYYbH, BZCYYbG, and BZCYYbHG electrolytes, respectively; **(e)** Raman spectra of the BZCYYb, BZCYYbH, BZCYYbG, and BZCYYbHG electrolytes after the pretreatments in 30% CO_2-30% H_2O-Ar at 650 °C for 100 h; and **(f)** TGA curves for BZCYYb, BZCYYbH, and BZCYYbHG electrolytes cooled from 800 to 200 °C in pure CO_2.

First attention is primarily drawn to the density and sintering performance of electrolytes in PCCs during the fabrication process.[16] Entropy strategies for addressing

electrolyte issues related to sinterability are carried out. The BZCYYb, BZCYYbH, BZCYYbG and BZCYYbHG ceramics were successfully synthesized according to the mixing entropy (ΔS_{mix}) for further properties and electrochemical measurements (**Figure 1a and S1**). When sintered at 1450 °C for 5 h, the relative densities of BZCYYb, BZCYYbH, BZCYYbG, and BZCYYbHG membranes reached 93.5%, 92.2%, 94.2%, and 95.4% measured by the Archimedes' method, respectively.[31] Also observed by the surface scanning electron microscope (SEM) images (**Figure 1b**), all samples exhibited dense surfaces with no apparent pore, which appears to be fully densified at 1450 °C. Thus, the sintering temperature of the electrolyte pellets was fixed at 1450 °C for 5 h. After interacting under an extreme condition of 30% CO_2 and 30% H_2O in Ar for 100 h, the surface morphology of the BZCYYbHG sample was smoother than that of BZCYYb **(Figure 1c)**. The results of all electrolyte samples comparatively suggest that the electrolytes with a higher entropy can maintain a relatively robust surface against CO_2 and H_2O. In analyses of the SEM images in **Figure 1b** and **Figure S2**, the mean grain size was a criterion for the sintering performance and density of the electrolytes (**Figure 1d**). The BZCYYbG and BZCYYbHG perovskite prompts the growth of the particles with larger average sizes of 1.01 and 1.12 μm than BZCYYb and BZCYYbHf, respectively. The surface deposited carbonate, and formation of hydroxide or/and nano-carbonates can be accurately detected by Raman spectra (**Figure 1e**). Raman spectra demonstrate that the peaks at 1060 cm^{-1} are likely associated with the $BaCO_3$.[11, 32] The intensities of the $BaCO_3$ peaks from BZCYYb to BZCYYbHG are weakened, consistent with the SEM results. However, the peak at 583 cm^{-1} belonging to β-$Ba(OH)_2$ did not appear in these Ba-containing perovskite electrolytes.[23, 33] Considering the more reactive characterization of electrolytes with CO_2, thermogravimetric analysis (TGA) measurements were further examined in pure CO_2 during the realistic cell operating temperatures of 800-200 °C (**Figure 1f**). The full desorption on the sample surface was carried out in N_2 from room temperature to 800 °C, then switched to pure CO_2 to examine the chemical stability (**Figure S3**). The BZCYYbH perovskite can weaken the CO_2 adsorption or/and carbonate formation

compared to BZCYYb, and a better CO_2 tolerance was achieved for BZCYYbHG. In summary, the BZCYYbHG possesses the best sinterability and chemical stability against H_2O and CO_2 among four electrolyte oxides, which further investigated its structural properties.

Structural characterization

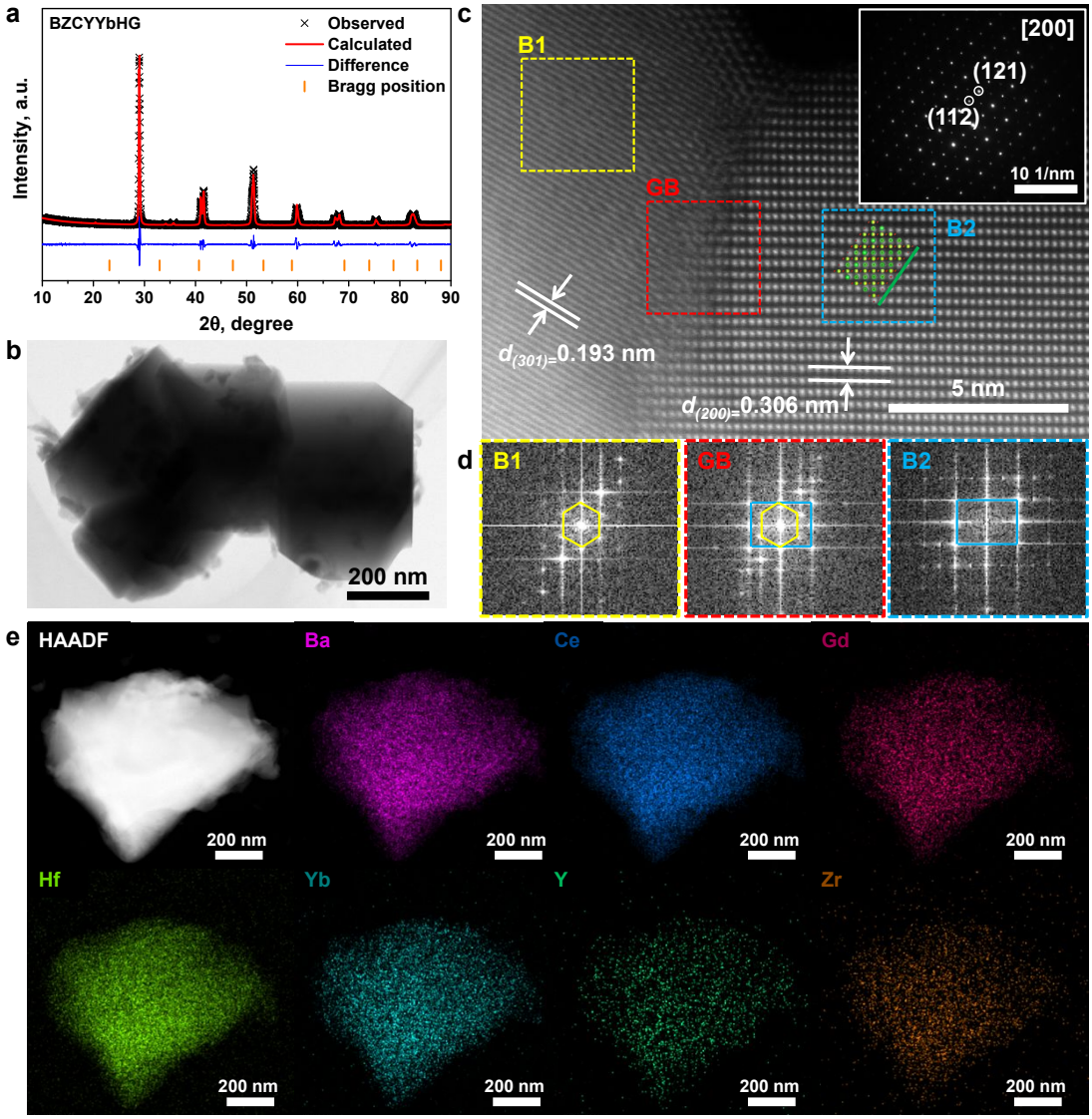

Figure 2. Structure of BZCYYbHG. (a) A Rietveld XRD refinement of the as-synthesized BZCYYbHG sample; **(b)** STEM image of the selected BZCYYbHG grain; **(c)** Aberration-corrected TEM (AC-TEM) image of the BZCYYbHG, inset is SAED pattern of BZCYYbHG along the [200] zone axis aligned parallel to the electron beam. The green arrow corresponding to the [200] zone axis of the sample; **(d)** FFT patterns

of the selected areas of bulk1 (B1, left yellow), grain boundary (GB, middle red), and bulk2 (B2, right blue) in (c); and **(e)** EDX mappings of the corresponding elements in the selected BZCYYbHG grain.

Refinement results from the crystal structure of BZCYYbHG demonstrate that the as-synthesized BZCYYbHG has orthorhombic perovskite structure (a=6.12840 Å, b=8.80938 Å, and c=6.15894 Å) with the space group of I*mma* (GOF=1.67), similar to the BZCYYb (GOF=0.63), BZCYYbH (GOF=0.50), and BZCYYbG (GOF=0.57) (**Figure 2a**, **Figure S4** and detailed parameters are shown in **Table S1**).[31] The actual atomic ratio of BZCYYbHG powder was examined as $Ba_{1.011}Zr_{0.067}Ce_{0.676}Y_{0.059}Yb_{0.062}Hf_{0.061}Gd_{0.064}O_{3-\delta}$ by inductively coupled plasma-mass spectrometry (ICP-MS), which was close to the nominal stoichiometric ratio (**Table S2**). As shown in **Figure 2b**, the scanning transmission electron microscopy (STEM) image demonstrates that the BZCYYbHG exhibits a particle size of 500-600 nm. To gain an atomic-scale observation of the entropy structure, aberration-corrected transmission electron microscope (AC-TEM) and selected area electron diffraction (SAED, inset) patterns were conducted for BZCYYbHG (**Figure 2c**). Two main lattice planes with diffraction distances of 1.93 and 3.06 Å were observed, corresponding to the (301) and (200) planes of the BZCYYbHG, respectively. **Figure 2c** (inset) shows the SAED pattern of the BZCYYbHG grain along the [200] zone axis. Two superlattice reflections of the (121) and (112) planes were observed, consistent with the XRD diffraction results. **Figure 2d** displays the fast Fourier transform (FFT) patterns of the region boxed in bulk1 (B1, yellow), grain boundary (GB, red), and bulk2 (B2, blue), respectively. The patterns were indexed according to perovskite-type unit cell, and the lattice parameters were calculated based on the SAED patterns. The A-site cations of the orthorhombic perovskite exhibit a special stacking by the green line (B2) along the [200] direction, differing from that around the B1 area. Thus, the 0.6-0.8 nm thick intergranular film is formed between two different bulks via the two competing interactions, which is recognized as the grain boundary of the grain (**Figure 2c)**.[34] The

ε_{xx} strain maps from geometric phase analysis (GPA) show the apparent existence of strip-like tensile strain on the grain boundary (**Figure S5**). Such nanometer-scale GBs should be optimized in electrolyte materials due to their much lower conductivity than the bulk conductivity. It has been reported by Nie *et al.* that the diffusion and mobility of ions via the grain boundary in ZnO-Bi_2O_3 are faster when the grain boundary transforms from disorder/amorphism to order.[35] Based on the FFT patterns of B1 and B2, a clear and overlaid superlattice on the GB was observed (**Figure 2d**, middle), implying that the issue of low GB conductivity is promising to be alleviated inside the BZCYYbHG grain. The high-angle annular dark-field (HAADF) image and energy-dispersive X-ray spectroscopy (EDX) (**Figure 2e**) show that the element distribution seems to be homogeneous within the BZCYYbHG grain at the nanoscale.

Electrochemical properties of electrolytes

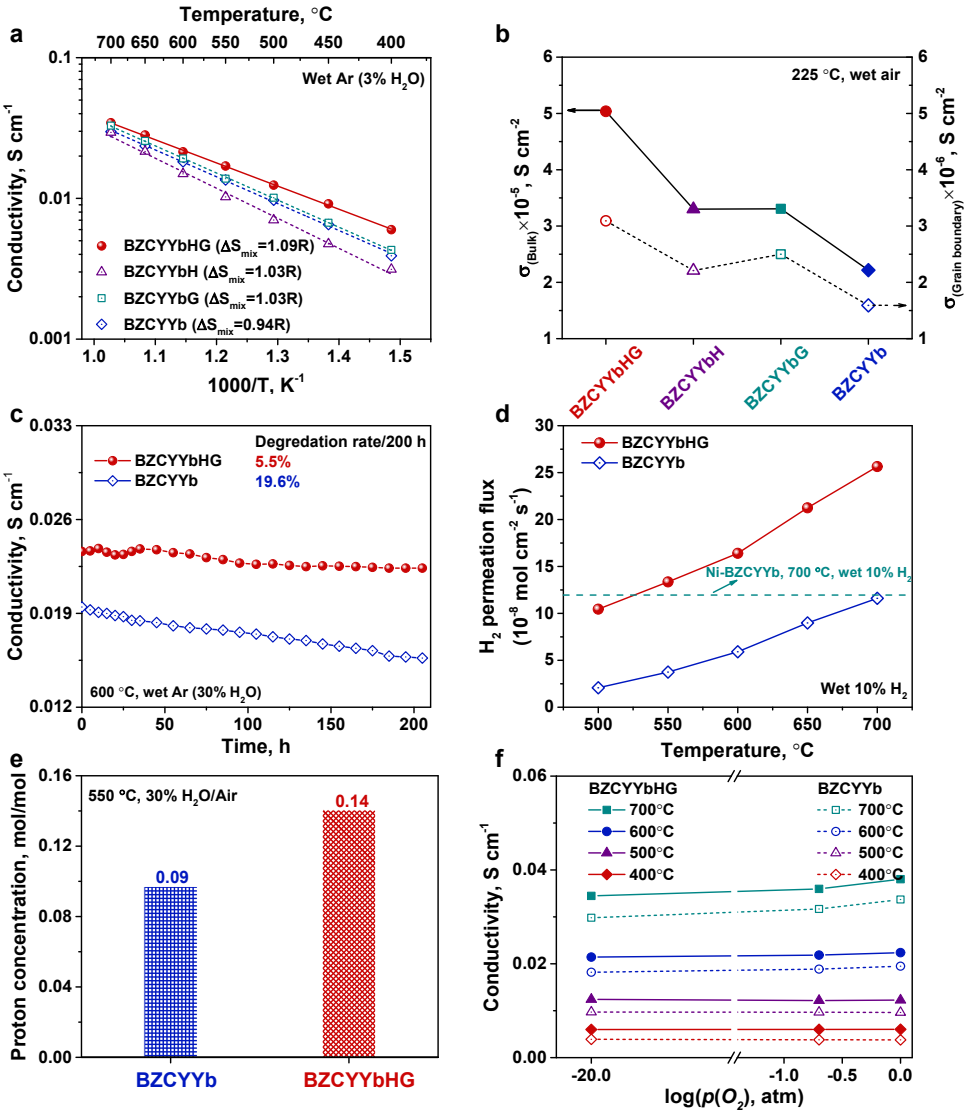

Figure 3. Investigation of the electrochemical properties of electrolytes with increasing entropy. (a) Arrhenius plots of conductivities for BZCYYb, BZCYYbH, BZCYYbG, and BZCYYbHG electrolytes, respectively; **(b)** Bulk and grain boundary conductivities of BZCYYb, BZCYYbH, BZCYYbG, and BZCYYbHG electrolytes under humidified air (3% H_2O) at 225 °C, respectively; **(c)** The conductivity stability of BZCYYb and BZCYYbHG electrolytes in wet Ar (30% H_2O) at 600 °C; **(d)** Hydrogen permeation fluxes of BZCYYb and BZCYYbHG dense membranes in wet 10% H_2-N_2 (3% H_2O) at 500-700 °C; **(e)** The proton concentrations of BZCYYb and BZCYYbHG dense membranes measured by the Karl-Fischer titration method; and **(f)** Conductivities of BZCYYb and BZCYYbHG as a function of p_{O_2} at 400-700 °C.

The conductivities of dense BZCYYb, BZCYYbH, BZCYYbG, and BZCYYbHG electrolytes were measured using electrochemical impedance spectroscopy (EIS) in wet argon (3% H_2O) at 400-700 °C. All those electrolytes performed typical activation energy (E_a) for proton conduction in the range of 0.31-0.40 eV. As found by Luo *et al.*[25] and Amsif *et al.*[36], the larger lattice-free volume and slighter lattice distortion are beneficial for the ionic conductivity of the perovskite electrolytes. The lattice-free volume of BZCYYb gets increased by several dopants with larger ionic radii (such as Gd^{3+}, Hf^{4+} and Er^{3+}), which can facilitate the ionic diffusions. The higher sintering density of BZCYYbHG electrolyte can supply more efficient proton transport, which leads to higher ionic conductivity. As displayed in **Figure 3a**, the BZCYYbHG electrolyte exhibits the highest conductivities of 0.012 and 0.006 S cm^{-1} at 500 and 400 °C, which were better than those of the state-of-the-art proton-conducting BZCYYb electrolyte (0.010 and 0.004 S cm^{-1} at 500 and 400 °C). The conductivities of the $BaZr_{1/6}Ce_{1/6}Y_{1/6}Yb_{1/6}Hf_{1/6}Gd_{1/6}O_{3-\delta}$ ($BZ_{1/6}C_{1/6}Y_{1/6}Yb_{1/6}H_{1/6}G_{1/6}$) with a higher entropy (ΔS_{mix}=1.79) were also examined; the value at 500 °C was only 7.35×10^{-5} S cm^{-1} due to the decrease of Ce contents (**Figure S6**). The ohmic resistances (R_o) of the electrolytes are separated into the bulk and grain boundary (GB) resistance by frequency range at low temperatures (≤ 250 °C) (**Figure S7**). As calculated by each resistance at different frequency ranges, the bulk conductivities of electrolytes are higher than their grain boundary conductivities (**Figure 3b**). The bulk and GB conductivities are correspondingly improved with the entropy increased from BZCYYb to BZCYYbHG electrolyte. Compared to the BZCYYb, the excellent sinterability and higher density of the BZCYYbHG may promote the proton conduction within the grain bulk and decrease the grain boundary resistance. High steam concentration (over 10% H_2O) has gradually become the essential operation condition encountered in proton ceramic electrolysis cells, which is a critical challenge for the water tolerance of air electrodes and electrolytes. **Figure 3c** displays the conductivity variations of the BZCYYb and BZCYYbHG electrolytes during long-term exposure (205 h) to the

highly humidified Ar (30% H_2O). The conductivity of the BZCYYbHG electrolyte was more stable, as validated by a lower degradation rate of 5.5% than that (19.6%) for BZCYYb. Additionally, the dense membranes of BZCYYb and BZCYYbHG electrolytes with a thickness of 0.6 mm were fabricated for hydrogen permeation (**Figure 3d**). The hydrogen flux of our tested BZCYYb at 700 °C was highly close to that of the Ni-BZCYYb as reported in the literature.[37] The hydrogen fluxes of the BZCYYbHG were two-fold higher than those of the BZCYYb at the same temperature and condition of wet 10% H_2-N_2 (3% H_2O). The calculated proton conductivities of BZCYYb and BZCYYbHG were slightly lower than their conductivities tested in wet Ar (3% H_2O) via EIS but at the same order of magnitudes (**Figure S8**). The main reason for conductivity discrepancies is that proton ceramic electrolytes show mixed proton and oxygen ion conductivities when tested in wet Ar, while approaching pure proton conductivity under hydrogen permeation tests. The oxygen vacancy concentrations of the BZCYYb and BZCYYbHG electrolytes were examined via the electron paramagnetic resonance (EPR) measurements. As shown in **Figure S8**, the BZCYYbHG samples have a slightly higher paramagnetic signal signature compared to BZCYYb, which implies a higher concentration of surface oxygen vacancies. More oxygen vacancies of BZCYYbHG can favor the formation of proton defects via the hydration reaction for faster proton conduction than BZCYYb.[25] When pretreated in the hydrated condition of wet air (30% H_2O) at 550 °C, the hydrated proton concentration of the dense electrolyte membranes can be precisely detected via the Karl-Fischer titration.[38] As shown in **Figure 3e**, the proton concentration of the BZCYYbHG was 0.14 mol H^+ per mol BZCYYbHG, which was higher than that of the state-of-the-art BZCYYb (0.09 mol H^+ per mol BZCYYb). The result confirmed that more oxygen vacancies of BZCYYbHG can favor the formation of proton defects via the hydration reaction for faster proton conduction than BZCYYb. Additionally, density functional theory (DFT) calculations (**Supplementary Note 1**) indicate that the higher configurational entropy of mixing at the B-site cations in BZCYYbHG compared to BZCYYb slightly reduces the hydrogen adsorption energy (**Figure S9**,

Table S3-S5, –2.29 eV versus –3.03 eV, respectively). This suggests a higher incorporation rate of protons or hydrogen atoms into bulk BZCYYbHG than BZCYYb. Then, to further understand the impact of proton conduction, we evaluated the diffusion barriers of protons in bulk BZCYYb and BZCYYbHG (**Figure S10** and **Table S6**). The results show that proton diffusion in high-entropy BZCYYbHG occurs faster than in BZCYYb, with average proton diffusion barriers of 0.27 eV and 0.47 eV, respectively, which are consistent with the experimental activation energies of 0.29 eV and 0.34 eV (**Figure S11**). This computational finding supports the higher proton conductivity of BZCYYbHG than BZCYYb, which is attributed from the higher configurational entropy of mixing at the B-site cations. Protonic ceramics have generally mixed proton, oxygen ion, and electron-hole conductivity, and the electronic charge carrier transference number was measured under oxidizing atmospheres (**Figure 3f**).[39] The conductivities at 400 and 500 °C were independent of the variation of p_{O_2}, while those at 600 and 700 °C were dramatically influenced (**Figure 3f** and **S12**). Among them, when the p_{O_2} increased from oxygen deficiency to pure oxidation at 600 and 700 °C, BZCYYbHG and BZCYYbH exhibited relatively slighter changes in the conductivities than BZCYYbG, similar to BZCYYb (**Figure 3f** and **S12**). The ionic transference number (t_{ion}) represents the ratio of the actual ion-conducting contributions to the theoretical value under cell operating conditions. As shown in **Figure S13**, the obtained t_{ion} approached unity at a low temperature of 500 °C, while electron-hole conducting on the oxidizing side led to the decreasing t_{ion} at elevated temperatures. Since the BZCYYbHG can possess the highest t_{ion} and reasonable open circuit voltages (OCVs) during the typical PCC operating temperatures (400-700 °C), BZCYYbHG perovskite is selected as the best candidate for the electrolyte and anode ceramics for further PCC fabrications.

Single-cell performance and durability tested in H_2, NH_3, and CH_4

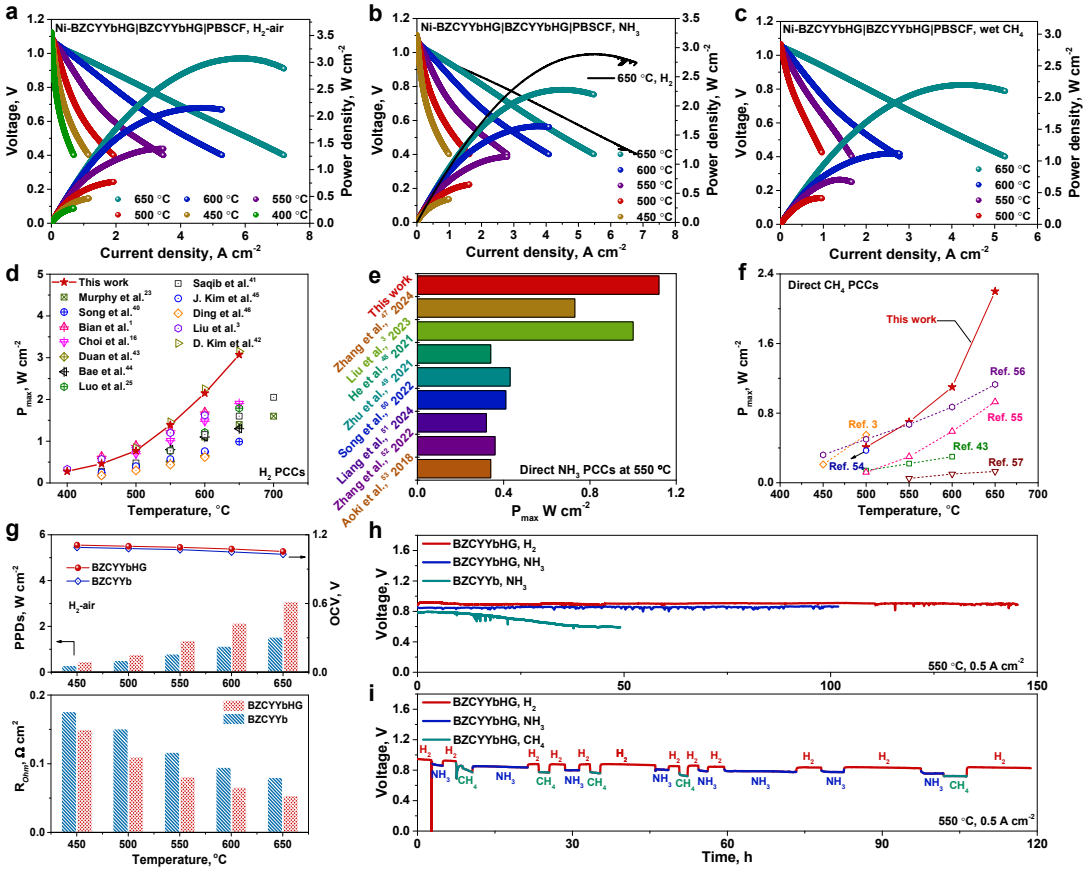

Figure 4. Electrochemical performance and durability of the single cells tested in H_2, NH_3 and CH_4. (**a-c**) Current density-voltage (I-V) and current density-power (I-P) curves of the BZCYYbHG cells measured in H_2 at 400-650 °C (**a**), in NH_3 at 450-650 °C (**b**), and in CH_4 at 500-650 °C (**c**), respectively; (**d-f**) Comparisons of fuel-cell P_{max} fueled by three fuels of H_2, NH_3, and CH_4 with the literature data, (**d**) H_2 (**Table S7**)[1, 3, 16, 23, 25, 40-46], (**e**) NH_3 at 550 °C (**Table S8**)[3, 47-53], and **(f)** CH_4 (**Table S9**)[3, 43, 54-57]; **(g)** Comparisons on OCV, PPDs and R_{ohm} of the BZCYYbHG cell and the BZCYYb cell fueled in H_2 at 450-650 °C; **(h)** Stability of the BZCYYbHG cell and BZCYYb cell at applied current density of 0.5 A cm^{-2} and 550 °C fueled by H_2 and NH_3, respectively; and **(i)** Cycling operation of the BZCYYbHG cell among multi-fuels of H_2, NH_3 and CH_4 at 0.5 A cm^{-2} and 550 °C.

A PCC was fabricated by a phase inversion process for the measurements of the electrochemical performance and stability,[58] with the configuration of a straight porous Ni-BZCYYbHG anode supported layer (ASL), a fine anode functional layer (AFL), a

dense BZCYYbHG electrolyte (thickness of ~6 μm), and a $PrBa_{0.5}Sr_{0.5}Co_{1.5}Fe_{0.5}O_{6-\delta}$ (PBSCF) cathode (**Figure S14**, denoted as the BZCYYbHG cell). The BZCYYb and BZCYYbHG electrolytes both showed excellent compatibility with NiO, which has been examined by the XRD patterns of the fuel electrodes after high-temperature calcination (**Figure S15**). When the Ni-BZCYYbHG anode was fed to H_2 and the PBSCF cathode was exposed to air, a high maximum peak power density (P_{max}) of 2.15 W cm^{-2} was achieved at 600 °C (**Figure 4a**). The BZCYYbHG cell displayed a low ohmic resistance (R_{ohm}) of 0.06 Ω cm^2 at 600 °C under OCV conditions (**Figure S16**). The PCC has demonstrated an outstanding advantage of fuel flexibility compared to polymer electrolyte fuel cells and proton exchange membrane fuel cells,[6, 10] which was also measured using ammonia and methane in this work. When H_2 was first fed into the anode, the BZCYYbHG cell achieved a P_{max} of 2.90 W cm^{-2} with a R_{ohm} of 0.05 Ω cm^2 and a R_p of 0.017 Ω cm^2 at 650 °C (**Figure 4b** and **S17**). Switching the fuel to ammonia (NH_3), a lower P_{max} of 2.28 W cm^{-2} with an increased R_{ohm} of 0.065 Ω cm^2 and R_p of 0.036 Ω cm^2 at the same temperature (**Figure 4b** and **S17**). Such larger resistance in NH_3 can be ascribed to the partial dilution of H_2 concentration at the vicinity of active sites on the anode. After directly interacting with ammonia, the BZCYYbHG ceramics in the anode are robust without the observation of nanogaps like BZCYYb as reported (**Figure S18**).[49] Methane, a typical hydrocarbon fuel, was directly utilized for power generation to examine the coking tolerance of Ni-BZCYYbHG. We also measured the electrochemical performance of the BZCYYbHG cell in wet methane (with 10% H_2O) at 500-650 °C (**Figure 4c**). Based on the high catalytic activity of nickel (Ni) particles for methane reforming at high temperatures, a high P_{max} of 2.19 W cm^{-2} was obtained at 650 °C. Meanwhile, the P_{max} of the cell presented a large degradation from 2.19 to 1.11, 0.70, and 0.41 W $cm^{-2,}$ with temperatures dropping from 650 to 600, 550, and 500 °C. The main contribution to the largely decreasing power density in wet CH_4 at low temperatures is the dramatically rising R_p from the Ni-based anode, as disclosed by EIS data (**Figure S19**). The cell performance in CH_4 at low temperatures can be effectively improved by enhancing the catalytic activity of the

Ni-based anode, such as infiltration of highly active metallic catalysts and modification of the anode catalytic layer.[3, 56] In addition, three different comparisons of cells used H_2 (**Table S7**),[1, 3, 16, 23, 25, 40-46] NH_3 (**Table S8**),[3, 47-53] and CH_4 (**Table S9**)[3, 43, 54-57] as fuels are taken with many advanced and high-performance PCCs reported recently to demonstrate the outstanding performance advantage of our fabricated PCC. Due to high conductivity and durability of the BZCYYHG electrolyte, durable and active Ni-BZCYYbHG anode, and excellent ORR activity of PBSCF cathode, our cell performances in H_2 and NH_3 fuels are among the best in comparison with many excellent PCFCs reported recently (**Figure 4d**, **4e**, **Table S7** and **S8**).[1, 3, 16, 23, 25, 40-53] Despite the insufficient catalytic activity of Ni-based anode on steam methane reforming below 550 °C, our cell performances in CH_4 are also comparable to the PCFCs with the infiltration of highly active catalysts on the anode at intermediate temperatures (**Figure 4f** and **Table S9**).[3, 43, 54-57]

To further demonstrate the promise of the BZCYYbHG cell, we facilitated trustworthy comparisons on the electrochemical performance of the cell with the state-of-the-art BZCYYb electrolyte, Ni-BZCYYb anode, and PBSCF cathode (denoted as the BZCYYb cell) (**Figure 4g** and **S20**). As summarized in **Figure 4g**, the P_{max} of the BZCYYb cell was 1.54, 1.14, 0.8, 0.51, and 0.29 W cm^{-2} at 650, 600, 550, 500, 450 °C in H_2, much lower than those of the BZCYYbHG cell under the same conditions. The higher OCVs and lower R_{ohm} of the BZCYYbHG cell were achieved than the BZCYYb cell at 450-650 °C, which is likely attributed to the higher densification and excellent proton conductivity of the BZCYYbHG electrolyte than the BZCYYb electrolyte (**Figure 4g**). As for the differences in the polarization resistances (R_p), the high conductivity of the BZCYYbHG anodic ceramics and the well-contacted interface of the electrolyte and electrodes may lead to slight decreases in the R_p of the BZCYYbHG cell. The detailed peak power densities of the BZCYYb cell fueled by H_2, NH_3, and wet CH_4 were summarized in **Table S10** for comparisons (**Figure S20-22**). The cell stability becomes increasingly significant for the next-generation PCCs either in H_2 or NH_3. Zhu *et al.*[49] reported that a direct ammonia-fueled PCFC with the BZCYYb

electrolyte exhibited a dramatic drop in the output voltages only for 15 hours at an applied current density of 0.5 A cm^{-2} and 650 °C. Liu *et al.*[3] reported that a high peak power density of 0.7 W cm^{-2} was obtained for the cell with the BZCYYb electrolyte at 500 °C in NH_3, but the more important cell stability was not conducted at intermediate temperature. Here, we evaluated the durability of the BZCYYbHG cell directly fueled by hydrogen and pure ammonia at 550 °C. The BZCYYb cell can perform a relatively stable operation for 120 h in H_2 at 0.5 A cm^{-2} and 550 °C (**Figure S23**). However, the poor durability of the BZCYYb cell was obtained within 49 h in NH_3 (**Figure 4h**), which was similar to the results reported by Zhu *et al*.[49] Determined by the SEM image on the Ni-BZCYYb anode (**Figure S24**), the formation of nanogap was occurred at the BZCYYb anode ceramic phase after short-term exposure to pure NH_3. Differing from the poor durability of the BZCYYb cell, the BZCYYbHG cell exhibited stable operations in H_2 and NH_3 for 145 and 102 h, respectively (**Figure 4h**). The BZCYYbHG cell exhibited relatively stable operation in wet CH_4 at 0.3 A cm^{-2} and 600 °C for 30 h, while the BZCYYb cell showed a fast and lasting voltage degradation within 7 h for a comparison (**Figure S25**). To further elucidate the performance degradation using methane, Raman spectra were conducted for the surface of the Ni-BZCYYb and Ni-BZCYYbHG anodes after the short-term stabilities (**Figure S26**). The higher intensity of peaks belonging to $BaCO_3$ (1060 cm^{-1}), D band (1357 cm^{-1}), and G band (1590 cm^{-1}) was observed on the surface of Ni-BZCYYb anode compared to Ni-BZCYYbHG anode.[32] Considering the excellent stability of the BZCYYbHG cell using three humidified fuels of H_2, NH_3 and CH_4, the multi-fuel cycling operation was further evaluated among these fuels at 0.5 A cm^{-2} and 550 °C (**Figure 4i**). When wet methane was first flowed to the Ni-BZCYYbHG fuel electrode, the voltage of the BZCYYbHG cell was degraded lastingly within 2 h owing to relatively low methane conversion of Ni catalysts at 550 °C. Subsequently, the cell performance was slightly decreased compared to the original voltage of 0.87 V initially fueled by NH_3, as an indicator of recovered voltage of 0.85 V by switched NH_3 fuel. After 119 h fast-switched multi-fuels cycling, the cell voltage was finally decreased to 0.83 V in H_2, but still operated

stably among H_2, NH_3 and CH_4. By comparison, the BZCYYb cell exhibited worse stability for 29 h during the same multi-fuel cycling, especially in wet CH_4 (**Figure S27**). The main factor for such unstable operation is the dramatic performance degradation of the BZCYYb cell when the fuel was switched to wet CH_4, likely due to the worse catalytic activity. The excellent mechanical strength and chemical stability of the BZCYYbHG cell exhibited a promising potential for the next-generation PCCs with high fuel flexibility.

Electrolysis performance, durability, and reversible cell operation measurements

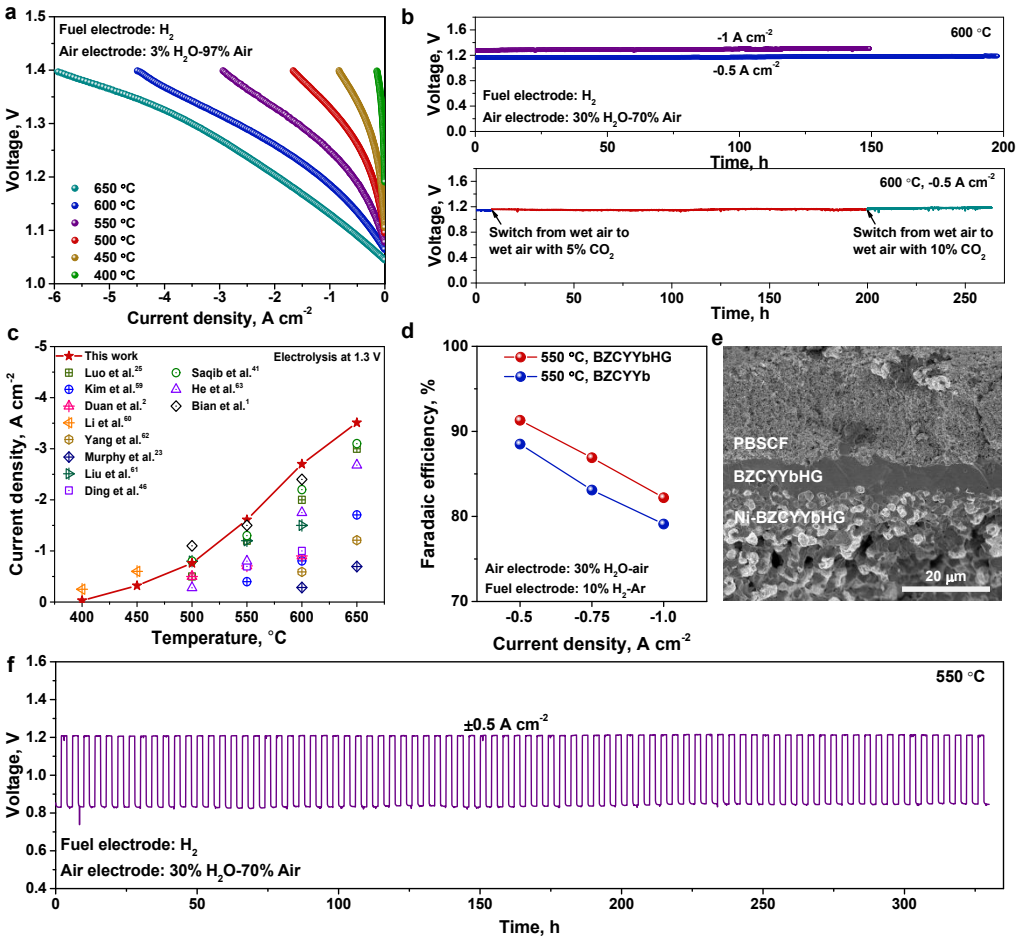

Figure 5. **Evaluations on electrolysis performance and durability tested under an atmosphere containing H_2O and CO_2. (a)** I-V curves of the BZCYYbHG cell in electrolysis at 400-650 °C; **(b)** Electrolysis stability of the BZCYYbHG cell tested under the current densities of -1 and -0.5 A cm^{-2} at 600 °C in humidified (30% H_2O) air (top) and wet air containing 0%, 5% and 10% CO_2 concentrations (bottom); (**c**) Comparison on current densities at 1.3V of our PCC with literature values at 400-700

°C (**Table S11**);[1, 2, 23, 25, 41, 46, 59-63] (**d**) Faradaic efficiency of the BZCYYbHG cell at 550 °C. The fuel electrode is fueled by 10% H_2-Ar, and the air electrode is exposed to air containing 30% H_2O; (**e**) Cross-sectional SEM image of the BZCYYbHG cell after operation on a reversible cycling mode; and (**f**) reversible cycling operation of the PCC under a fast-switching (2 h) mode applied at ±0.5 A cm^{-2} and at 550 °C.

The electrolysis mode of PCC is a reverse fuel-cell process for efficiently converting electrical energy to chemical energy, potentially enabling grid-scale energy storage and clean hydrogen production from intermittent renewable energy. The electrolysis performance of the BZCYYbHG cell was evaluated at 400-650 °C, as shown in **Figure 5a**. Specifically, the current densities of -3.51, -1.61, and -0.32 A cm^{-2} were obtained under the applied voltage of 1.3 V at 650, 550, and 450 °C, respectively. The electrolysis stabilities of the BZCYYbHG cell were conducted under the applied current densities of -0.5 and -1 A cm^{-2} at 600 °C, when the BZCYYbHG electrolyte was exposed to air containing 30% H_2O (**Figure 5b**, top). As shown in **Figure 5b** (top), the output voltage of the cell showed a slight increase from 1.17 to 1.18 V at -0.5 A cm^{-2} and 600 °C for 197 h. When the current density increased to -1 A cm^{-2}, the cell voltage remained stable at 1.30 V within 150 h, suggesting the BZCYYbHG electrolyte performed excellent durability under a high current density and harsh steam concentration. As proof of the CO_2 durability of BZCYYbHG electrolyte, the cell electrolysis was lastly operated under a humidified air atmosphere with increasing CO_2 concentrations from 0 to 5% and 10% at -0.5 A cm^{-2} and 600 °C (**Figure 5b**, bottom). When the 5% CO_2 concentration was first introduced into wet air (3% H_2O) in the chamber of air electrode, the cell voltage increased from the original 1.14 V to 1.16 V, and remained at 1.16 V for 200 h. When the CO_2 concentration rose from 5% to 10%, the cell voltage reached 1.17 V and remained stable for the next 64 h. When 5% CO_2 was introduced for the electrolysis operation of the BZCYYb cell, the voltage of the BZCYYb cell showed a dramatic increase from 1.18 to 1.28 V at -0.5 A cm^{-2} and 600 °C within 18.5 h (**Figure S28**). Shown in **Figure S29** are XRD patterns and SEM

images of the BZCYYb and BZCYYbHG samples after treatments in 30% CO_2-30% H_2O-40% air at 550 °C for 100 h. After exposure to high-concentration CO_2 and H_2O, the obvious peaks belonging to the carbonate were observed on the XRD patterns of the BZCYYb and BZCYYbHG electrolytes (**Figure S29a**). According to the ratio of the peak intensity of $BaCO_3$ (I_{BaCO3}) and perovskite ($I_{perovskite}$), the BZCYYbHG exhibited relatively more robust structural tolerance against H_2O and CO_2 than BZCYYb (**Figure S29b and S29c**). Compared to the BZCYYbHG, more nanoparticles were found on the surface of the BZCYYb electrolyte at the same scale of 2 μm, making it more difficult to distinguish the grain bulk and boundary (**Figure S29d** and **S29e**). The obtained electrolysis stabilities demonstrate that the BZCYYbHG electrolyte possesses excellent durability for H_2O- and CO_2-containing conditions, which can be extensively applied in CO_2 electrolysis using PCC. **Figure 5c** displays the current densities at 1.3 V of the BZCYYbHG cell compared to other PCCs with outstanding electrolysis performance in recent literature, indicating that the electrolysis performance of our BZCYYbHG cell is among the top (**Table S11**).[1, 2, 23, 25, 41, 46, 59-63]

Most of the prior PCCs have performed low Faradaic efficiency due likely to ionic transport loss or defect reactions in the electrolyte and at the triple-phase interface.[6] As shown in **Figure 5d**, the Faradaic efficiency of the BZCYYbHG cell was 91.3, 86.9, and 82.2 % under the applied current densities of 0.5, 0.75, and 1.0 A cm^{-2} at 550 °C, higher than those (88.5, 83.1, and 79.1 %) of the BZCYYb cell. With the temperature increased to 600 °C, the Faradaic efficiency of the cell was inevitably decreased (**Figure S30a**), and the corresponding H_2 production rates detected by gas chromatography were also shown in **Figure S30b**. Thus, establishing the electrolyte material design of the entropy concept minimizes electronic leakage for a more efficient BZCYYbHG cell. The reversible cycling of the PCCs needs durable cell architecture and fast proton transport inside the electrodes and electrolyte, especially at a relatively low temperature of 550 °C (**Figure S31**). **Figure 5e** displays that the cell configuration after the 82 times reversible cycling was well-adhesive between electrodes and BZCYYbHG electrolyte. The fabricated BZCYYbHG cell conducted a

fast (2 h) cycling operation between the fuel-cell mode and electrolysis mode at current densities of ±0.5 A cm^{-2} at 550 °C (**Figure 5f**). No degradation in the cell performance was obtained within 330 h, suggesting the excellent stability of the BZCYYbHG cell for efficient energy utilization and storage.

Conclusions

In summary, we have developed the BZCYYbHG perovskite as an electrolyte for highly fuel-flexible and reversible PCCs. Compared to the state-of-the-art BZCYYb electrolyte, BZCYYbHG electrolyte demonstrates higher conductivity of 0.017 S cm^{-1} at 550 °C, greater sinterability, enhanced structural durability against H_2O and CO_2, and exceptional cell performance and stability. DFT calculations indicate that the higher configurational entropy of mixing at the B-site cations slightly reduces the hydrogen adsorption energy, demonstrating a higher incorporation rate of protons or hydrogen atoms into the electrolyte bulk. Single cells with the developed BZCYYbHG electrolyte deliver decent peak densities at 550 °C of 1.39 W cm^{-2} in H_2, 1.12 W cm^{-2} in NH_3, and 0.7 W cm^{-2} in wet CH_4, respectively. Moreover, our PCC achieves a current density of -1.61 A cm^{-2} at 1.3 V and 550 °C in steam electrolysis mode. More importantly, our PCCs demonstrate durable fuel-cell operations at 550 °C in H_2 for 145 h, NH_3 for 102 h and wet CH_4 for 30 h, steam electrolysis at 600 °C in harsh humid (30% H_2O) air for 197 h and wet air containing CO_2 (up to 10%) for 264 h, and reversible cycling at 550 °C and ±0.5 A cm^{-2} for 330 h, respectively. The entropy engineering on the electrolyte in this study highlights the potential for fabricating high-performance and durable PCC using high flexibility and reversibility.

Experimental procedures

Fabrication of electrolyte and electrode powders

$BaZr_{0.06}Ce_{0.7}Y_{0.06}Yb_{0.06}Hf_{0.06}Gd_{0.06}O_{3-\delta}$ (BZCYYbHG), $BaZr_{0.075}Ce_{0.7}Y_{0.075}Yb_{0.075}Hf_{0.075}O_{3-\delta}$ (BZCYYbH), $BaZr_{0.075}Ce_{0.7}Y_{0.075}Yb_{0.075}Gd_{0.075}O_{3-\delta}$ (BZCYYbG), and $BaZr_{0.1}Ce_{0.7}Y_{0.1}Yb_{0.1}O_{3-\delta}$ (BZCYYb) electrolyte powders were synthesized by solid-state sintering process.

Briefly, stoichiometric amounts of $BaCO_3$, HfO_2, ZrO_2, CeO_2, Y_2O_3, Yb_2O_3 and Gd_2O_3 were ball-milling in ethanol for 4 h according to the BZCYYbHG formula. The mixture was dried at 70 °C for 24 h, calcined at 1375 °C for 5 h in air at a fast-heating rate of 10 °C min^{-1} and then crushed into fine electrolyte powder. The as-synthesized electrolyte powder was then ball-milled with NiO, polyethersulfone (PESf), polyvinyl pyrrolidone (PVP), and N-Methyl pyrrolidone (NMP) for 24 h to obtain the fuel electrode slurry. The $PrBa_{0.5}Sr_{0.5}Co_{1.5}Fe_{0.5}O_{6-\delta}$ (PBSCF) air electrode powder was synthesized by a sol-gel method using $Pr(NO_3)_3 \cdot 6H_2O$, $Ba(NO_3)_2$, $Sr(NO_3)_2$, $Co(NO_3)_2 \cdot 6H_2O$, $Fe(NO_3)_3 \cdot 9H_2O$ as the precursors. The gel was dried at 300 °C for 5 h, and calcined at 950 °C for 5 h to obtain the final electrode powder.

Cells fabrication

The above-mentioned fuel electrode slurry was dip-coated on a glass rod with a diameter of 4 mm, fully immersed in water for 10 h to obtain the raw tube. The raw tube was sintered at 1000 °C to obtain the substrate. The fuel electrode functional layer slurry comprised 50 wt% electrolyte powder, 50 wt% NiO, organic dispersant and binder, and the electrolyte layer slurry included electrolyte powder, organic dispersant and binder. The fuel electrode functional layer and electrolyte layer slurries were dip-coated on the anode substrate, and then co-sintered at 1450 °C for 5 h to achieve the half cells. The air electrode slurry was composed of the PBSCF powder, ethyl cellulose, and terpineol at a weight ratio of 1:0.04:0.76. The air electrode slurry was printed onto the electrolyte surface of the half cells with an effective area of 0.21 cm^{-2}, and then sintered at 950 °C for 2 h.

Electrolyte pellet conductivity test

The ionic conductivity of the electrolytes was measured by the EIS of the electrolyte pellets. The grain bulk and boundary conductivity were analyzed by fitting the impedance spectra using ZView software. The electrolyte powders were dry-pressed into pellets with a diameter of 13.0 mm and calcined at 1450 °C for 5 h to obtain dense electrolyte pellets. The dense pellets were polished with sandpapers to obtain a smooth surface. The silver paste was applied on both sides of the pellets to collect the current

using a brush. The ohmic resistance of the electrolyte pellets was measured by EIS under a humidified argon atmosphere (3% H_2O) with a flowing rate of 30 mL min^{-1} at 400-700 °C and 225 °C. The EIS spectra were collected using an electrochemical potentiostat (AMETEK PARSTAT MC 200).

Hydrogen detection

The hydrogen permeation fluxes were accurately detected by the thermal conductivity detector (TCD) of the gas chromatograph (GC-7820, Huifen Instrument Co., Ltd). The GC was equipped with a TDX-01 packed column and 5A molecular sieve for TCD. For the hydrogen permeation tests of the electrolyte pellets, the inlet gas was wet 10% H_2-N_2 at a rate of 30 mL min^{-1}. The outlet gas was Ar gas at a rate of 30 mL min^{-1} and directly fixed to the automatic sampling valve of GC. The electrolyte powders were dry-pressed into pellets with a diameter of 13.0 mm and calcined at 1450 °C for 5 h to obtain dense electrolyte pellets. The dense pellets were polished by sandpaper to obtain a smooth surface with a thickness of 0.6 mm. The electrolyte pellets were sealed with glass sealant (AREMCO 552), and silver paste was applied on both sides of the pellets. For Faradaic efficiency tests, the fuel electrode was fueled by 10% H_2-Ar at a rate of 60 mL min^{-1}, and the air electrode was provided by humidified air (30% H_2O) at a rate of 60 mL min^{-1}. The Faradaic efficiency is obtained by dividing the total charge transported for the electrolytes by the quantity of electric charge for hydrogen production. The Faradaic efficiency was calculated as:

$$FE_{H_2} = \frac{n_{H_2,measured}}{n_{H_2,theoretical}} = \frac{n_{H_2,measured}}{I\times(n\times F)^{-1}} \times 100\% \quad (1)$$

$n_{H2,measured}$ is the measured hydrogen production rate (unit is mol s^{-1}) by a GC, I is the current (unit is A), n is 2.

Sample characterization

Proton concentrations of the electrolyte pellets were determined by the Karl-Fischer titration method. The dense electrolyte pellets were pre-treated in wet air (30% H_2O) at 550 °C for 100 h, and then annealed in dry air. The water contained in the samples was evaporated by an ADP-512S furnace kept at 1000 °C and was swept by N_2 flow (200 mL min^{-1}) into an MKC-710S titration cell. ICP measurement was tested for the actual

stoichiometric ratio of samples (Aglient 5110). The EPR measurements (Bruker EMXplus-6/1) were conducted for comparing the oxygen vacancy concentrations of the electrolytes. The crystal structures of as-prepared materials were obtained by Bruker D8 advance (Germany Bruker) X-ray diffraction instrument using Cu Kα radiation (λ = 0.15406 nm). Raman spectroscopy on the surfaces of fuel electrodes and electrolytes was characterized by a Horiba Raman spectrophotometer (LabRAM HR Evolution). The microstructure, morphology, and element distribution of samples were examined by SEM (Hitachi SU8010, Japan) and aberration corrected (AC)-TEM (Spectra 200, Thermo Fisher). TGA measurements were conducted on the STA 449 F3 instrument (NETZSCH) in pure CO_2 atmosphere with a cooling rate of 5 °C min^{-1}.

Electrochemical tests

For the electrochemical tests of single cells, the fuel electrode was fueled by H_2, NH_3 and wet CH_4 (10% H_2O) at a fixed rate of 60 mL min^{-1}. The air electrode was exposed to ambient air in fuel-cell mode, while being flowed by wet air (3 and 30% H_2O) and wet air containing 5 and 10% CO_2 at a rate of 60 mL min^{-1} in electrolysis mode. The I-V-P curves, EIS, and stability of the cells were tested, all using an electrochemical potentiostat (PARSTAT MC 200).

Computational methods.

Periodic density functional theory (DFT) calculations were conducted using the Vienna *Ab initio* simulation package (VASP)[64, 65] to investigate the enhanced performance of the BZCYYbHG electrolyte compared to BZCYYb. The projector augmented wave (PAW)[66] method and the Perdew-Burke-Ernzerhof (PBE) exchange-correlation functional[67] were employed, with Gaussian smearing of 0.05 eV and a kinetic energy cutoff set of 520 eV. The climbing image nudged elastic band (CI-NEB) method[68] was applied to calculate the barrier heights of bulk proton transfer. Detailed computational methods are provided in **Supplementary Note 2**.

Author contributions

Y. C., Z. S., and Y. M. C. conceived, designed, and supervised the project. F. H., K. X.,

Y. X. and Y. H. carried out the fabrication of the powders, cells, and conducted data analysis of all electrochemical experiments. Y. M. C., and K. S. conducted the density functional theory (DFT) calculations. H. T. and L. Z. conducted AC-TEM. F. H., Y. C., and Y. M. C. contributed to writing the paper.

Acknowledgements

This work was financially supported by the Introduced Innovative R&D Team of Guangdong (2021ZT09L392), the National Natural Science Foundation of China (22179039 and 22005105), the Fundamental Research Funds for the Central Universities (2022ZYGXZR002), the Pearl River Talent Recruitment Program (2019QN01C693), the Guangdong Basic and Applied Basic Research Foundation (2021A1515010395), and Zijin Mining Group Co., Ltd (5405-ZC-2023-00008). Y.M.C. acknowledges the National Science and Technology Council (NSTC Grant No. 111-2221-E-A49-003-MY3), the National Center for High-performance Computing (NCHC), and the Higher Education Sprout Project of the National Yang-Ming Chiao Tung University and Ministry of Education (MOE), Taiwan. DFT calculations were performed using the resources of the Center for Functional Nanomaterials, which is a U.S. DOE Office of Science Facility, at Brookhaven National Laboratory under Contract No. DE-SC0012704.

Declaration of interests

The authors declare no competing interests.

References and Notes

1. W. Bian, W. Wu, B. Wang, W. Tang, M. Zhou, C. Jin, H. Ding, W. Fan, Y. Dong and J. Li, *Nature*, 2022, **604**, 479-485.
2. C. Duan, R. Kee, H. Zhu, N. Sullivan, L. Zhu, L. Bian, D. Jennings and R. O'Hayre, *Nature Energy*, 2019, **4**, 230-240.
3. F. Liu, H. Deng, D. Diercks, P. Kumar, M. H. A. Jabbar, C. Gumeci, Y. Furuya, N. Dale, T. Oku and M. Usuda, *Nature Energy*, 2023, **8**, 1145-1157.

4. Z. Liu, Y. Bai, H. Sun, D. Guan, W. Li, W.-H. Huang, C.-W. Pao, Z. Hu, G. Yang and Y. Zhu, *Nature Communications*, 2024, **15**, 472.
5. F. He, M. Hou, D. Liu, Y. Ding, K. Sasaki, Y. Choi, S. Guo, D. Han, Y. Liu and M. Liu, *Energy & Environmental Science*, 2024, **17**, 3898-3907.
6. C. Duan, J. Huang, N. Sullivan and R. O'Hayre, *Applied Physics Reviews*, 2020, **7**.
7. C. Duan, R. J. Kee, H. Zhu, C. Karakaya, Y. Chen, S. Ricote, A. Jarry, E. J. Crumlin, D. Hook and R. Braun, *Nature*, 2018, **557**, 217-222.
8. H. An, H.-W. Lee, B.-K. Kim, J.-W. Son, K. J. Yoon, H. Kim, D. Shin, H.-I. Ji and J.-H. Lee, *Nature Energy*, 2018, **3**, 870-875.
9. S. Zhai, H. Xie, P. Cui, D. Guan, J. Wang, S. Zhao, B. Chen, Y. Song, Z. Shao and M. Ni, *Nature Energy*, 2022, **7**, 866-875.
10. L. Yang, S. Wang, K. Blinn, M. Liu, Z. Liu, Z. Cheng and M. Liu, *Science*, 2009, **326**, 126-129.
11. F. He, M. Hou, F. Zhu, D. Liu, H. Zhang, F. Yu, Y. Zhou, Y. Ding, M. Liu and Y. Chen, *Advanced Energy Materials*, 2022, 2202175.
12. J. Zhang, S. Ricote, P. V. Hendriksen and Y. Chen, *Advanced Functional Materials*, 2022, **32**, 2111205.
13. K. Pei, Y. Zhou, K. Xu, H. Zhang, Y. Ding, B. Zhao, W. Yuan, K. Sasaki, Y. Choi and Y. Chen, *Nature communications*, 2022, **13**, 2207.
14. Y. Zhou, E. Liu, Y. Chen, Y. Liu, L. Zhang, W. Zhang, Z. Luo, N. Kane, B. Zhao, L. Soule, Y. Niu, Y. Ding, H. Ding, D. Ding and M. Liu, *ACS Energy Letters*, 2021, **6**, 1511-1520.
15. Z. Liu, Y. Song, X. Xiong, Y. Zhang, J. Cui, J. Zhu, L. Li, J. Zhou, C. Zhou and Z. Hu, *Nature Communications*, 2023, **14**, 7984.
16. M. Choi, J. Paik, D. Kim, D. Woo, J. Lee, S. J. Kim, J. Lee and W. Lee, *Energy & Environmental Science*, 2021, **14**, 6476-6483.
17. D. Kim, K. T. Bae, K. J. Kim, H.-N. Im, S. Jang, S. Oh, S. W. Lee, T. H. Shin and K. T. Lee, *ACS Energy Letters*, 2022, **7**, 2393-2400.

18. Z. Luo, Y. Zhou, X. Hu, W. Wang, Y. Ding, W. Zhang, T. Li, N. Kane, Z. Liu and M. Liu, *Small*, 2023, **19**, 2208064.
19. M. Wang, W. Wu, Y. Lin, W. Tang, G. Gao, H. Li, F. F. Stewart, L. Wang, Y. Yang and D. Ding, *ACS Applied Energy Materials*, 2023, **6**, 8316-8326.
20. H. Matsumoto, Y. Kawasaki, N. Ito, M. Enoki and T. Ishihara, *Electrochemical and Solid-State Letters*, 2007, **10**, B77.
21. S. Haile, G. Staneff and K. Ryu, *Journal of Materials Science*, 2001, **36**, 1149-1160.
22. L. He, F. Zhang, Y. Xuan, L. Zhang, H. Gao, H. Pan, S. Lian, M. Wang, J. Yin and X. Chen, *Journal of The Electrochemical Society*, 2021, **168**, 034517.
23. R. Murphy, Y. Zhou, L. Zhang, L. Soule, W. Zhang, Y. Chen and M. Liu, *Advanced Functional Materials*, 2020, **30**, 2002265.
24. M. Yashima, T. Tsujiguchi, Y. Sakuda, Y. Yasui, Y. Zhou, K. Fujii, S. Torii, T. Kamiyama and S. J. Skinner, *Nature communications*, 2021, **12**, 556.
25. Z. Luo, Y. Zhou, X. Hu, N. Kane, T. Li, W. Zhang, Z. Liu, Y. Ding, Y. Liu and M. Liu, *Energy & Environmental Science*, 2022, **15**, 2992-3003.
26. R. Witte, A. Sarkar, R. Kruk, B. Eggert, R. A. Brand, H. Wende and H. Hahn, *Physical Review Materials*, 2019, **3**, 034406.
27. F. He, F. Zhu, D. Liu, Y. Zhou, K. Sasaki, Y. Choi, M. Liu and Y. Chen, *Materials Today*, 2023, **63**, 89-98.
28. S. C. Kim, J. Wang, R. Xu, P. Zhang, Y. Chen, Z. Huang, Y. Yang, Z. Yu, S. T. Oyakhire and W. Zhang, *Nature Energy*, 2023, **8**, 814-826.
29. C. Oses, C. Toher and S. Curtarolo, *Nature Reviews Materials*, 2020, **5**, 295-309.
30. R. D. Shannon, *Foundations of Crystallography*, 1976, **32**, 751-767.
31. F. He, Z. Teng, G. Yang, C. Zhou, D. Guan, S. Chen, R. Ran, W. Wang, W. Zhou and Z. Shao, *Journal of Power Sources*, 2020, **460**, 228105.
32. K. Xu, H. Zhang, W. Deng, Y. Liu, Y. Ding, Y. Zhou, M. Liu and Y. Chen, *Science Bulletin*, 2023, **68**, 2574-2582.

33. H. Lutz, W. Eckers, G. Schneider and H. Haeuseler, *Spectrochimica Acta Part A: Molecular Spectroscopy*, 1981, **37**, 561-567.
34. D. R. Clarke, *Journal of the American Ceramic Society*, 1987, **70**, 15-22.
35. J. Nie, C. Hu, Q. Yan and J. Luo, *Nature Communications*, 2021, **12**, 2374.
36. M. Amsif, D. Marrero-Lopez, J. Ruiz-Morales, S. Savvin, M. Gabás and P. Nunez, *Journal of Power Sources*, 2011, **196**, 3461-3469.
37. M. Liu, W. Sun, X. Li, S. Feng, D. Ding, D. Chen, M. Liu and H. C. Park, *International journal of hydrogen energy*, 2013, **38**, 14743-14749.
38. D. Han, X. Liu, T. S. Bjørheim and T. Uda, *Advanced Energy Materials*, 2021, **11**, 2003149.
39. H. Zhu, S. Ricote, C. Duan, R. P. O'Hayre, D. S. Tsvetkov and R. J. Kee, *Journal of The Electrochemical Society*, 2018, **165**, F581.
40. Y. Song, Y. Chen, W. Wang, C. Zhou, Y. Zhong, G. Yang, W. Zhou, M. Liu and Z. Shao, *Joule*, 2019, **3**, 2842-2853.
41. M. Saqib, I.-G. Choi, H. Bae, K. Park, J.-S. Shin, Y.-D. Kim, J.-I. Lee, M. Jo, Y.-C. Kim and K.-S. Lee, *Energy & Environmental Science*, 2021, **14**, 2472-2484.
42. D. Kim, I. Jeong, S. Ahn, S. Oh, H. N. Im, H. Bae, S. J. Song, C. W. Lee, W. Jung and K. T. Lee, *Advanced Energy Materials*, 2024, **14**, 2304059.
43. C. Duan, J. Tong, M. Shang, S. Nikodemski, M. Sanders, S. Ricote, A. Almansoori and R. O'Hayre, *Science*, 2015, **349**, 1321-1326.
44. K. Bae, D. H. Kim, H. J. Choi, J. W. Son and J. H. Shim, *Advanced Energy Materials*, 2018, **8**, 1801315.
45. J. H. Kim, J. Hong, D. K. Lim, S. Ahn, J. Kim, J. K. Kim, D. Oh, S. Jeon, S. J. Song and W. Jung, *Energy & Environmental Science*, 2022, **15**, 1097-1105.
46. H. Ding, W. Wu, C. Jiang, Y. Ding, W. Bian, B. Hu, P. Singh, C. J. Orme, L. Wang, Y. Zhang and D. Ding, *Nature Communications*, 2020, **11**, 1907.
47. H. Zhang, K. Xu, Y. Xu, F. He, F. Zhu, K. Sasaki, Y. Choi and Y. Chen, *Energy & Environmental Science*, 2024, **17**, 3433-3442.

48. F. He, Q. Gao, Z. Liu, M. Yang, R. Ran, G. Yang, W. Wang, W. Zhou and Z. Shao, *Advanced Energy Materials*, 2021, **11**, 2003916.

49. L. Zhu, C. Cadigan, C. Duan, J. Huang, L. Bian, L. Le, C. H. Hernandez, V. Avance, R. O'Hayre and N. P. Sullivan, *Communications Chemistry*, 2021, **4**, 121.

50. Y. Song, J. Chen, M. Yang, M. Xu, D. Liu, M. Liang, Y. Wang, R. Ran, W. Wang and F. Ciucci, *Small*, 2022, **18**, 2200450.

51. M. Liang, Y. Song, B. Xiong, D. Liu, D. Xue, L. Shen, K. Shi, Y. Song, J. Li, Q. Niu, M. Xu, F. Ciucci, W. Zhou and Z. Shao, *Advanced Functional Materials*, 2024, **n/a**, 2408756.

52. H. Zhang, Y. Zhou, K. Pei, Y. Pan, K. Xu, Y. Ding, B. Zhao, K. Sasaki, Y. Choi and Y. Chen, *Energy & Environmental Science*, 2022, **15**, 287-295.

53. Y. Aoki, T. Yamaguchi, S. Kobayashi, D. Kowalski, C. Zhu and H. Habazaki, *Global Challenges*, 2018, **2**, 1700088.

54. Y. Chen, B. DeGlee, Y. Tang, Z. Wang, B. Zhao, Y. Wei, L. Zhang, S. Yoo, K. Pei and J. H. Kim, *Nature Energy*, 2018, **3**, 1042-1050.

55. D. Konwar, B. J. Park, P. Basumatary and H. H. Yoon, *Journal of Power Sources*, 2017, **353**, 254-259.

56. K. Hong, M. Choi, Y. Bae, J. Min, J. Lee, D. Kim, S. Bang, H.-K. Lee, W. Lee and J. Hong, *Nature communications*, 2023, **14**, 7485.

57. L. Lei, J. M. Keels, Z. Tao, J. Zhang and F. Chen, *Applied Energy*, 2018, **224**, 280-288.

58. Y. Pan, H. Zhang, K. Xu, Y. Zhou, B. Zhao, W. Yuan, K. Sasaki, Y. Choi, Y. Chen and M. Liu, *Applied Catalysis B: Environmental*, 2022, **306**, 121071.

59. J. Kim, A. Jun, O. Gwon, S. Yoo, M. Liu, J. Shin, T.-H. Lim and G. Kim, *Nano Energy*, 2018, **44**, 121-126.

60. W. Li, B. Guan, L. Ma, S. Hu, N. Zhang and X. Liu, *Journal of Materials Chemistry A*, 2018, **6**, 18057-18066.

61. Z. Liu, Z. Tang, Y. Song, G. Yang, W. Qian, M. Yang, Y. Zhu, R. Ran, W.

Wang and W. Zhou, *Nano-Micro Letters*, 2022, **14**, 217.

62. S. Yang, S. Zhang, C. Sun, X. Ye and Z. Wen, *ACS Applied Materials & Interfaces*, 2018, **10**, 42387-42396.
63. F. He, Y. Zhou, T. Hu, Y. Xu, M. Hou, F. Zhu, D. Liu, H. Zhang, K. Xu and M. Liu, *Advanced Materials*, 2023, 2209469.
64. G. Kresse and J. Hafner, *Physical Review B*, 1993, **47**, 558-561.
65. G. Kresse and J. Furthmuller, *Physical Review B*, 1996, **54**, 11169-11186.
66. P. E. Blöchl, *Physical Review B*, 1994, **50**, 17953-17979.
67. J. P. Perdew, K. Burke and M. Ernzerhof, *Physical Review Letters*, 1996, **77**, 3865-3868.
68. G. Henkelman, B. P. Uberuaga and H. Jónsson, *J. Chem. Phys.*, 2000, **113**, 9901-9904.

Data availability

The data supporting this article have been included as part of the ESI.†